Ink-substrate interactions during 3D printing revealed by time-resolved coherent X-ray scattering

M. Torres Arango [a], Y. Zhang [a], C. Zhao [b], R. Li [a], G. Doerk [c], D. Nykypanchuk [c], Y-c. K. Chen-Wiegart [b, a], A. Fluerasu [a], L. Wiegart [a, *]

[a] National Synchrotron Light Source II, Brookhaven National Laboratory, 744 Brookhaven Avenue, Upton, NY 11973, USA
[b] Department of Materials Science and Chemical Engineering, Stony Brook University, 100 Nicolls Road, Stony Brook, NY 11794, USA
[c] Center for Functional Nanomaterials, Brookhaven National Laboratory, 735 Brookhaven Avenue, Upton, NY 11973, USA

ARTICLE INFO

ABSTRACT

Additive printing techniques are regarded as revolutionary and versatile methods of advanced device manufacturing, stemming from the possibility to pattern materials on a custom-based approach and the potential to create novel microstructures and achieve new functionalities. Despite these advantages, the inherent anisotropy of the printing process is a source of property gradients within the printed materials, often associated with variable and/or poor performance. Up to date, the evolutionary pathways associated with printing have largely remained unaddressed, mainly owing to the difficulty to study the transformations induced in the material during processing. Time-resolved coherent X-ray scattering techniques, such as X-ray photon correlation spectroscopy, enable the *in situ* study of transient nanoscale and mesoscale states in a large variety of materials, including amorphous ones, by directly accessing the most relevant timescales and length scales of their nanoscale and mesoscale dynamics, self-assembly, and mesostructure evolution. We conduct *in operando* studies of continuous-flow direct writing with colloidal inks, focusing on how the ink formulation and ink-substrate interactions affect the processes that determine the macroscopic properties of the printed materials. We find fundamental differences in the ink structural relaxations emerging from the primary colloid properties (monodisperse versus aggregated colloids) and the substrates surface energy and mechanical properties. Our work helps to reveal and quantify the basic science governing the evolution of 3D-printed materials during processing, ultimately improving engineering criteria for the design of printable materials.

Published by Elsevier Ltd.

1. Introduction

Additive manufacturing (AM) processes are considered as versatile and efficient deposition techniques that overcome issues of traditional subtractive manufacturing including materials waste and the need of dedicated specialized tools, in turn reducing the number of steps in processing and hence shortening product development times. Moreover, AM has enabled a whole new approach to materials synthesis where novel structures and new functionalities are realized [1,2]. Nevertheless, the intrinsic anisotropy associated with these processes becomes an important source of property gradients and defects in the fabricated components [3]. For example, the shear profile associated with the extrusion from the nozzle, as well as the shear associated with the deposition of a filament create property gradients across the filament. Such gradients may influence the pathway of the material all the way to solidification and can be reflected in the final nanoscale and mesoscale structure. Interlayer bonding, either between filaments or between a filament and substrate, is typically determined by interlayer diffusion and creates additional property gradients that depend on the processing pathway, for example, on the time between consecutive filament depositions [4]. Therefore, it is imperative to understand the effects of processing on the materials and identify the main relationships influencing their evolution.

Among the different AM printing techniques, continuous-flow direct writing (CDW) is of great interest across multiple technological fields owing to the wide range of processable ink viscosities and breadth of attainable microstructures [5-7]. In particular, in the fabrication of ceramics with application in energy [8,9],

biomedicine [2,10,11], and environmental remediation [12,13], CDW usually makes use of colloidal viscoelastic ink systems that are loaded in syringe-like cartridges and extruded through a nozzle following a computer programed trajectory [1,14,15]. Once patterned, the structures are generally subjected to curing and sintering treatments, where some of the ink precursors (commonly organic species) are removed and the material final microstructure is attained [11,16]. With such an approach, top-down and bottom-up synthesis techniques are often combined [17-19], providing further means for controlling the materials composition and species-colloid interactions, and hence materials properties. In this context, the role of processing should be acknowledged, not only from the perspective of the ink formulation and subsequent transformation during the synthesis but also including the deposition mechanism as an important means of microstructural control [20-23]. The final mesoscale structure of 3D printed materials is determined by properties of the materials involved, such as ink and substrate, and the non-equilibrium pathway from extrusion through deposition to solidification. While *ex situ* studies may allow for establishing some materials-processing-properties relationships, they cannot reveal the complex physical processes governing material transformation during 3D printing, such as shear during printing and subsequent structural relaxation, drying, and curing. Without such knowledge, a detailed understanding and multiscale physics modeling of the 3D printing of colloidal inks would remain elusive. This knowledge gap presents a roadblock for predictive modeling and transformative materials and process development based on computational simulations and exploration of the vast parameter phase space guided by artifical intelligence (AI) and machine learning (ML) methods. *In situ* experiments are an important step to expand our knowledge about materials under processing conditions such as CDW.

While synchrotron-based scattering techniques are being successfully applied to study (semi)crystalline polymers processed by fused filament fabrication [24,25], time-resolved coherent scattering in combination with increasingly fast detectors and customized experimental setups has only recently allowed the characterization of complex AM processes and their transient phenomena in polymer nanocomposites processed by CDW [21,26].

Specifically for CDW, a versatile platform for *in situ* characterization has been developed at the Coherent Hard X-ray scattering beamline (CHX-11ID) of the National Synchrotron Light Source II, Brookhaven National Laboratory [26], allowing the study of evolutive pathways of inks dynamics and structure rearrangement processes during the out-of-equilibrium stages [21,26]. This technical capability enables us to probe nanoscale and mesoscale length scales with sufficient time and spatial resolution *in situ/operando* and to resolve the multilength and timescale character of the events that take place during the out-of-equilibrium stages. We perform comparative studies using inks with monodisperse and branched (aggregated) colloidal fillers (often used as functional materials in inks for CDW) that are printed on substrates with different coatings (uncoated, hydrophobized SiO₂ and Crystalbond — a resin-like material) and investigate the differences of the ink-substrate interactions in relation with the colloid structure, as well as the systems free surface energy, roughness, and mechanical properties. The ink-substrate interactions play an important role in the local interfacial defect development, that constitute a critical aspect for printed devices such as battery electrodes and solar cells, where The substrate is acting as electrical contact [27-30]. In addition, in 'thin' single-layer printed structures, these interactions become more relevant as the materials may deform and collapse to accommodate stress-induced deformations associated with the materials solidification and densification processes.

With X-ray techniques, the timescales and length scales relevant to *in situ* experiments of CDW processes with colloidal inks are only accessible with scattering techniques. However, morphological information obtainable by scattering for weakly ordered (quasi amorphous) colloidal materials is limited. Certain findings in the dynamics (e.g. the presence of dynamic heterogeneities) may point toward the presence of mesoscale and macroscale structural defects in the final (cured) structure. Therefore, we conduct complementary *ex situ* imaging characterization, including X-ray nanotomography by transmission X-ray microscopy (TXM) and optical and electron microscopy of the final structure, supporting our conclusions about the mesoscale structure of the materials drawn from observations of dynamic phenomena during the printing process.

In section 2, we detail our experimental approach and theoretical basis for the *operando* X-ray photon correlation spectroscopy (XPCS) studies. In section 3, we discuss the results and draw connections between the properties of the substrates and ink systems; and their evolution regarding dynamics and mesostructure. We start by analyzing the out-of-equilibrium dynamics during printing and relaxation of the colloidal ink systems and investigate the development of dynamic heterogeneities during relaxation. We continue with the *in situ* structural analysis using small angle X-ray scattering (SAXS) and the *ex situ* structural analysis by electron and X-ray microscopy. Finally, we provide concluding remarks in section 4 and analyze the suitability and relevance of XPCS for the investigation of transient out-of-equilibrium processes in 3D printing using CDW.

2. Materials and methods

2.1. Ink systems

The prepared ink systems contain silica colloids, either of monodisperse (≈ 250 nm diameter, ink hereafter referred to as mono SiO₂) or aggregated (primary particle size ≈ 7 nm, ink hereafter referred to as branched SiO₂) nature, constituting the main solids loading in the formulations. The inks contain minimum amounts of methyl cellulose to increase their elasticity. All other constituents are considered as solvents in this work's discussion, refer Table 1.

The differences in ink composition reflect the specific colloid properties, requiring different amounts of stabilizers and dispersants to render inks with rheological properties appropriate for printing, refer Supplementary Information, Fig. S1. Further details on the ink formulation and characterization are available in Supplementary Information.

2.2. Substrate treatments and characterization

Three different substrates were used in the *operando* experiments, consisting of bare and thin film-coated Si wafers. The different coatings were sprayed onto 6 mm × 15 mm precut Si wafers (using a commercially available paint gun) to modify the surface properties (Table 3). The coatings consisted of a thin resin film (Crystalbond-509, Aremco) and a hydrophobic sol-gel fluorinated silica coating. For the former, a 15 wt% Crystalbond 509 solution in acetone was prepared, sprayed directly onto the wafer, and

Table 1
Ink composition and constituents in vol%.

Ink name	SiO$_2$	Water	Ethylene glycol	Diethanolamine	Methyl cellulose
Mono SiO$_2$	35.83	51.78	11.89	–	0.51
Branched SiO$_2$	16.41	45.73	33.90	2.75	1.21

allowed to dry without any further processing. For the hydrophobic coating, a variation of the sol-gel method by Kessman and Cairns [31] and Banerjee et al. [32] was used. Substrate characterization was performed in terms of wettability and surface morphology by advancing contact angle measurements and atomic force microscopy (AFM), refer Supplementary Information, Substrate Characterization section.

2.3. Printed structure ex situ characterization

Thermogravimetric analysis (TGA, PerkinElmer Pyris Diamond TG/DTA) of the inks was used to confirm the inks SiO$_2$ content and to investigate the room temperature solvent evaporation kinetics of deposited filaments, reproducing the experimental conditions during the *operando* experiments. X-ray and electron microscopy measurements were performed to obtain structural information complementary to the *operando* X-ray scattering data. The microscopy studies of the printed structures were performed after annealing the filaments for 20 min at 700 °C to remove organic species and facilitate focused-ion beam (FIB) sample preparation. Cylindrical samples of 20–30 μm diameter and ≈50 μm height for characterization by X-ray nanotomography were prepared using a lift-out process in a dual beam (Helios, Thermo Fisher Scientific Inc.) focused-ion beam and scanning electron microscopy system [33]. FIB milling was carried out to mill a cylindrical-shaped specimen from the interface between the printed ink and the substrate (after fully drying the filaments, they had no adhesion to the substrates), with the cylinder length axis being perpendicular to the deposition direction (Fig. 1a). Following the milling process, the lift-out process was carried out by gently attaching a micromanipulator to the top of the cylindrically milled sample to transfer the specimen onto a Pt sample mounting pin. Synchrotron-based nanotomography was conducted at the Full-field X-ray Imaging Beamline (FXI-18-ID) [34], National Synchrotron Light Source II, Brookhaven National Laboratory. Additional details are available in Supplementary Information.

2.4. Operando characterization by time-resolved coherent X-ray scattering

Operando characterization of the ink during printing, consecutive recovery, and partial curing by time-resolved coherent X-ray scattering was performed using an in-house built extrusion-based direct ink writing printer [26] at the Coherent Hard X-ray scattering (CHX) beamline 11-ID.

The filament deposition used a pressure-controlled syringe-piston system (Ultimus V, Nordson) with a 580 μm inner diameter conical nozzle (Nordson part-number: 7005009). The extrusion pressure and printhead speed were set to 55 kPa and 0.3 mm/s and 68 kPa and 0.2 mm/s for the mono SiO$_2$ and branched SiO$_2$ inks, respectively. Coated and uncoated wafers were mounted on the printbed using self-sticking adhesive tabs (Product no. 76760, Electron Microscopy Sciences), which allowed recovery of the wafers after filament deposition for further *ex situ* characterization. The height h from the substrate surface at which the filaments were probed by the X-ray beam was set to ≈50 μm by the vertical translation of the printer upon locating the substrate's surface via an absorption scan. X-ray scattering experiments were performed with a partially coherent X-ray beam with wavelength λ = 1.285 Å, focused to a spot size of ≈10 μm diameter, full width at half maximum (FWHM). Multiple optical cameras with varying resolution and field of view were used to monitor the deposition process, including an on-axis microscope, imaging the sample along the direction of the X-ray beam (Fig. 1a). For the filament deposition, the printhead of the printer was moved along the x-direction, keeping the printbed and deposited filament stationary during data acquisition (refer to coordinate system, Fig. 1a). By starting the data acquisition before the printhead crossing the X-ray beam, the intensity rise associated with the filament being deposited across the beam can be used to define the 'age' (t$_{age}$) of the material being probed, with the intensity rise corresponding to t$_{age}$ = 0 s (Fig. 1a, c). The total length of the extruded filaments was 13 mm, deposited symmetrically around the beam position. This corresponds to more than 20 s of deposition prior and after passing the X-ray beam, sufficient to avoid any effects due to the start or stop of the deposition. The evolution of the dynamics and structure of the filament was followed with a series of data sets, each adjusting acquisition and transmission parameters. A 50 μm horizontal shift of the sample position between consecutive data sets was introduced to avoid accumulation of X-ray dose in a single spot. The acquired data sets were used to characterize the out-of-equilibrium dynamics and structural evolution following extrusion and relaxation of the inks via XPCS and time-resolved SAXS. Printer controls and data acquisition were realized via the Bluesky software package [35], while two- and four-time correlation functions (variance χ), as well as radially averaged SAXS intensity curves were computed using Python-based code available at the CHX beamline [36].

The out-of-equilibrium dynamics associated with the extrusion, deposition, and consecutive relaxation and curing of the inks can be characterized by time-resolved (two-time) intensity-intensity correlation functions of the form [37,38],

$$G(Q, \Phi, t_1, t_2) = \frac{\langle I(Q, \Phi, t_1) \cdot I(Q, \Phi, t_2) \rangle_{Q', \Phi'}}{\langle I(Q, \Phi, t_1) \rangle_{Q', \Phi'} \cdot \langle I(Q, \Phi, t_2) \rangle_{Q', \Phi'}}, \quad (1)$$

where $I(Q, \Phi, t_i)$ is the intensity at time t$_i$ in the scattering pattern, measured at a detector pixel corresponding to an average wavevector amplitude $Q = 4\pi \sin(\theta)/\lambda$ and azimuthal angle Φ. The ensemble average $\langle \ldots \rangle_{Q', \Phi'}$ is performed over detector pixel in the range $Q' = Q \pm \Delta Q$ and $\Phi' = \Phi \pm \Delta \Phi$, where $\Delta Q = 0.002$ Å^{-1} and $\Delta \Phi = 10°$ for all data sets in this study. The two-time correlation function according to Eq. (1) is the most comprehensive way to describe the dynamics, as it represents the intensity-intensity
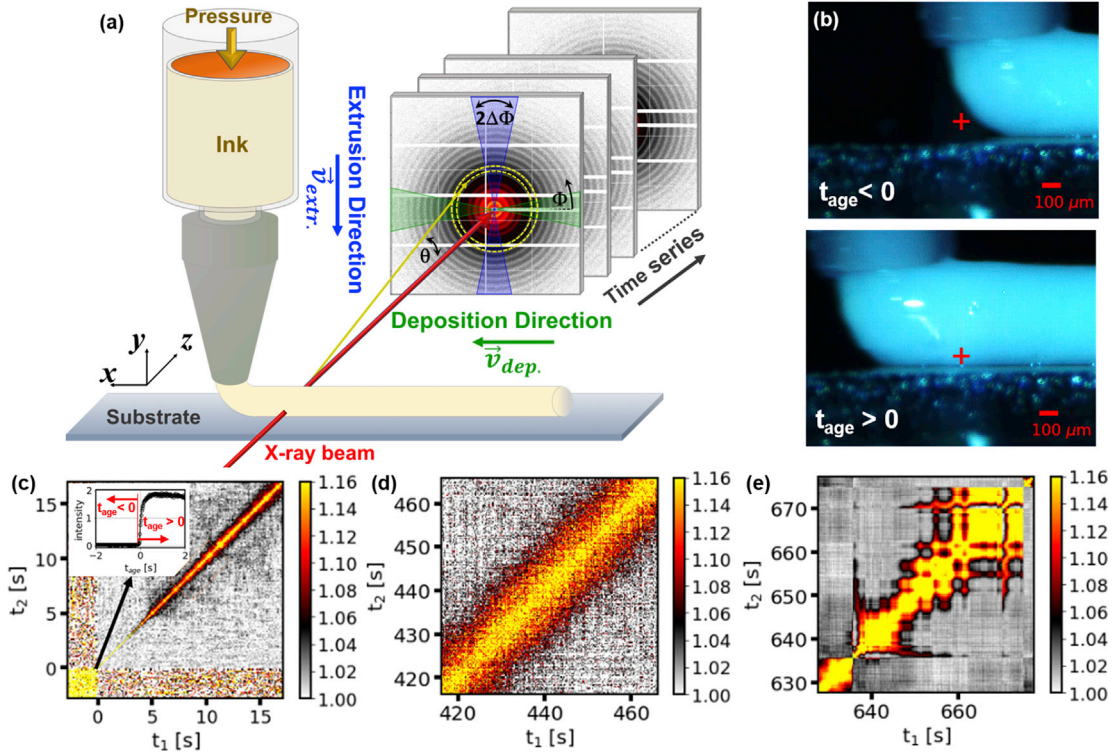
Fig. 1. (a) Schematic of the XPCS *operando* experiment, portraying the deposition and extrusion directions, as well as the definition of the azimuthal angle Φ and scattering angle 2θ. For a stable filament deposition, extrusion and deposition speeds need to match ($v_{extr.} = v_{dep.}$). (b) Optical microscope images acquired simultaneously with the X-ray scattering data of the representative stages of the deposition onset before ($t_{age} < 0$) and after ($t_{age} > 0$) crossing the X-ray beam (red cross marks the position of the X-ray beam) (c–e) Representative two-time correlation functions during (c) and post deposition (d, e). Inset in (c) depicts the intensity rise associated with the filament crossing the X-ray beam that defines $t_{age} = 0$. XPCS, X-ray photon correlation spectroscopy.

autocorrelations on a frame by frame basis, that is, without temporal averaging and with the time resolution of the frame rate used during data acquisition. Two-time correlation functions are therefore adequate to describe not only quasi-stationary but also out-of-equilibrium dynamics in particular. Further data analysis illustration is available as Supplementary Information, section S1. Experimental Details and Fig. S3. For limited time intervals $t_{age} \pm \Delta t_{age}$ over which the two-time correlation function describes a quasi-stationary state, one can average the two-time correlation function around an average aging time $t_{age} = (t_1 + t_2)/2$ to obtain 'aged' one-time correlation functions of the form [39]:

where β is a setup dependent contrast factor, determined by the coherence properties of the X-ray beam and the spatial sampling of the speckles. $\tau_0(Q, \Phi, t_{age})$ is the relaxation time quantifying the timescale of the dynamics. The compression exponent γ is characteristic for different types of dynamics, such as $\gamma = 1$ for Brownian diffusion, $\gamma < 1$ for subdiffusive, or $\gamma > 1$ for hyperdiffusive (ballistic) dynamics.

The aged one-time correlation functions (Eq. (3)) can quantitatively describe the out-of-equilibrium dynamics of samples with evolving timescales, as long as the time averages are kept short enough to capture the kinetics. However, they cannot describe

$$
g_2\left(Q, \Phi, t_{age}, \tau\right) = \left\langle \frac{\left\langle I\left(Q, \Phi, t_{age} - \frac{\tau}{2}\right) \cdot I\left(Q, \Phi, t_{age} + \frac{\tau}{2}\right)\right\rangle_{Q', \Phi'}}{\left\langle I\left(Q, \Phi, t_{age} - \frac{\tau}{2}\right)\right\rangle_{Q', \Phi'} \cdot \left\langle I\left(Q, \Phi, t_{age} + \frac{\tau}{2}\right)\right\rangle_{Q', \Phi'}} \right\rangle_{t_{age} \pm \Delta t_{age}}, \tag{2}
$$

with the lag time $\tau = |t_2 - t_1|$. While t_{age} progresses along the diagonal ($t_1 = t_2$) of the two-time correlation functions, the aged one-time correlation functions are essentially cuts with 'width' $2\Delta t_{age}$ perpendicular to this diagonal. Quantitative information about the dynamics can be obtained by fitting the aged one-time correlation functions to a Kohlrausch-Williams-Watts form [40],

$$
g_2\left(Q, \Phi, t_{age}, \tau\right) = 1 + \beta e^{-2(\tau/\tau_0)^{\gamma}}, \tag{3}
$$

larger fluctuations in $G(Q, \Phi, t_1, t_2)$ associated, for example, with the collective dynamics common in colloidal gels and emulsions [41–43]. Such collective dynamics can be expected to play a role in the solidification of the inks, when solvent evaporation and volume shrinkage drive the system toward jamming and an arrested state. Fluctuations in G arising from such type of dynamics can be quantified by its normalized variance [39,41]:

$$\chi(Q,\Phi,t_{age},\tau)=\frac{\langle G^2(Q,\Phi,t_{age},\tau)\rangle_{t_{age}\pm\Delta t_{age}}-\langle G(Q,\Phi,t_{age},\tau)\rangle^2_{t_{age}\pm\Delta t_{age}}}{[g_2(Q,\Phi,t_{age},\tau=0)-1]^2}$$

(4)

which can be related to the susceptibility χ_4 that characterizes spatial heterogeneity in the dynamics of glassy materials [39].

3. Results and discussion

3.1. Out-of-equilibrium dynamics (XPCS)

Wavevector-dependent two-time correlation functions are calculated according to Eq. (4) for the two principal Φ directions (Fig. 1a), namely along the extrusion direction (perpendicular to the substrate) and along the deposition direction (parallel to the substrate) [21]. Following the out-of-equilibrium dynamics of the ink, or more precisely of the colloids, which dominate the scattering signal due to their larger electron density as compared with that of the other ink constituents, multiple data sets were collected over ages in the range of 1500 s > t_{age} > 0 s, during and after deposition. For each consecutive data set, acquisition parameters were chosen according to the slowing dynamics while adjusting the transmission of the X-ray beam to stay below the determined threshold for beam damage. Representative two-time correlation functions spanning ages corresponding to the *in situ* deposition (filament crossing the X-ray beam, corresponding to $t_{age} = 0$ s determined by the step-like increase in scattering intensity, refer inset in Fig. 1c) to later stages, governed by slowing down dynamics and dynamic heterogeneities (Fig. 1e) are observed. Broadening of the two-time correlation function with elapsing time is indicative of a progressive reduction of the colloid mobility. At later times, the two-time correlation functions for the mono SiO_2 ink display heterogeneities, indicating dynamics governed by sudden dislocations and rearrangements in the ink nanostructure (Fig. 1e). This kind of temporal heterogeneities is typical of strong gels and jammed systems where the overcoming of multiple local maximum energy thresholds during the relaxation process gives rise to the observed fluctuating pattern [44]. While the initial trends described by the two-time correlation functions (onset and broadening) are common to both of the ink systems studied, the development of temporal heterogeneities is exclusive to the monodisperse colloid ink system over the investigated time frame. These heterogeneities are further investigated in section 3.2.

To quantify the evolving timescales of the dynamics, the two-time correlation functions are time averaged over relevant $t_{age} + \Delta t_{age}$ sections (Eq. (2)) that are then subsequently fitted according to Eq. (3) to extract the relaxation time τ_0, as well as the contrast β and compression exponent γ. As an example, a series of representative correlation functions $g_2(t_{age}, \tau\Phi, Q)$ is shown in Fig. 2a. The systematic shift toward longer relaxation times τ_0 with increasing t_{age} reflects the lower mobility of the colloids within the ink as time passes and the inks recover their gel structure and ultimately undergo a drying process driven by solvent (water) evaporation. A representative time evolution of γ (averaged over Q) for the mono SiO_2 and branched SiO_2 on the Crystalbond-coated substrate is shown in Fig. 2c, d, respectively. An evolution of the functional form of these correlation functions from an initially stretched ($\gamma < 1$) to a compressed ($\gamma > 1$) behavior is also evident, suggesting a transition from subdiffusive to hyperdiffusive dynamics.

For all investigated combination of inks and substrate coatings, the compression exponent γ depends only on Φ and t_{age} but is independent of Q (as shown in the inset of Fig. 2d). The branched SiO_2 ink exhibits subdiffusive dynamics ($\gamma \approx 0.7$) right after the deposition, which quickly evolves into hyperdiffusive dynamics with $\gamma \approx 1.5$ within 4.5 s < t_{age} < 15 s. In the intermediate regime, (4.5 s < t_{age} < 100 s) γ is about 1.5−1.75, before reapproaching $\gamma \approx 1.5$ for t_{age} > 100 s. Qualitatively, this evolution holds for the branched SiO_2 ink on all three different substrates. For the mono SiO_2 ink, the compression exponent right after deposition is $\gamma \approx 0.5$ and remains smaller than one up to t_{age} > 50 s. In the intermediate regime (280 s > t_{age} > 650 s), γ continues to increase, reaching values in the range 1.25 < γ < 1.75. It is noteworthy that for t_{age} > 280 s, the dynamics exhibit significant temporal heterogeneities, that is, the dynamics in this time window cannot be completely described by aged one-time correlation functions, which might contribute to this large observed spread of γ values. For t_{age} > 650 s, γ approaches values of $\approx 1.5–1.75$. The evolution of γ for the mono SiO_2 ink on all three substrates is qualitatively similar to the branched SiO_2 ink. However, the systematically smaller γ values observed along the extrusion direction (Fig. 2c) are exclusive to the Crystalbond-coated substrate. For the other two substrates, there is no appreciable dependence on the direction and the values follow the ones for the extrusion direction on the Crystalbond-coated substrate. Similar γ values ($\gamma \approx 2$) have also been reported for aerogel undergoing internal relaxation after the application of a strong localized deformation [39].

For both ink systems and all substrates, the contrast factor β determined from the fit of the aged two-time correlation functions at early ages is smaller than the contrast factor $\beta_0 \approx 0.16–0.17$ determined for the experimental setup using a static sample (porous glass, CoralPor®, SCHOTT). In addition, β exhibits a strong Q-dependence (refer insert of Fig. 2f), indicating that the sample dynamics at early ages contains some faster relaxation modes, with timescales faster than the minimum lag-time τ accessible in our experimental setup, and the observed β is the arrested decay of these non-ergodic dynamics. Such fast modes in concentrated colloidal systems are, for example, the 'rattling' of individual particles within the 'cage' formed by their nearest neighbors [45−47]. The height β of the initial plateau is related to the average amplitude or mean square displacement δ of these fluctuations by $\beta \propto \exp(-Q^2\delta^2/3)$ [41,48,49]. A fit of this relationship for the branched SiO_2 ink on the uncoated substrate at $t_{age} = 6.5$ s along the deposition direction is shown in the insert of Fig. 2f. The mean square displacements δ of these fast dynamic modes as a function of age for both ink systems on the uncoated substrates are shown in Fig. 2e, f. For the mono SiO_2 ink and $t_{age} < 1$ s, we find values of $\delta \approx 20$ nm and $\delta \approx 10$ nm in the deposition and extrusion directions, respectively. These values decrease with increasing age until β approaches β_0 for t_{age} > 300 s. A similar behavior is observed for the branched SiO_2 ink, with initial values of $\delta \approx 10$ nm and $\delta \approx 6$ nm for the deposition and extrusion direction, respectively, and β approaching β_0 for t_{age} > 400 s. For early ages right after the ink deposition ($t_{age} < 20$ s), both ink systems show large amplitude fluctuations along the deposition direction, with the amplitudes being about a factor of two larger for the mono SiO_2 ink. During deposition, the inks experience additional forces, such as the shear due to the interaction with the substrate and stretching (viscoelastic drag) along this direction. For short times afterward, the cages of nearest neighbor colloids may be asymmetric (stretched along the deposition direction) and allow fluctuations with non-isotropic amplitudes. This anisotropy quickly vanishes during the inks' relaxation and the reestablishment of the gel structure. The observed reduction of the amplitudes of the fast dynamic mode with t_{age} indicates an increasing solidification of the inks, accompanied by increasing storage modules G' [42,48], up to the point where the fast dynamic modes become completely frozen in, and the dynamics are completely shifted toward the timescales
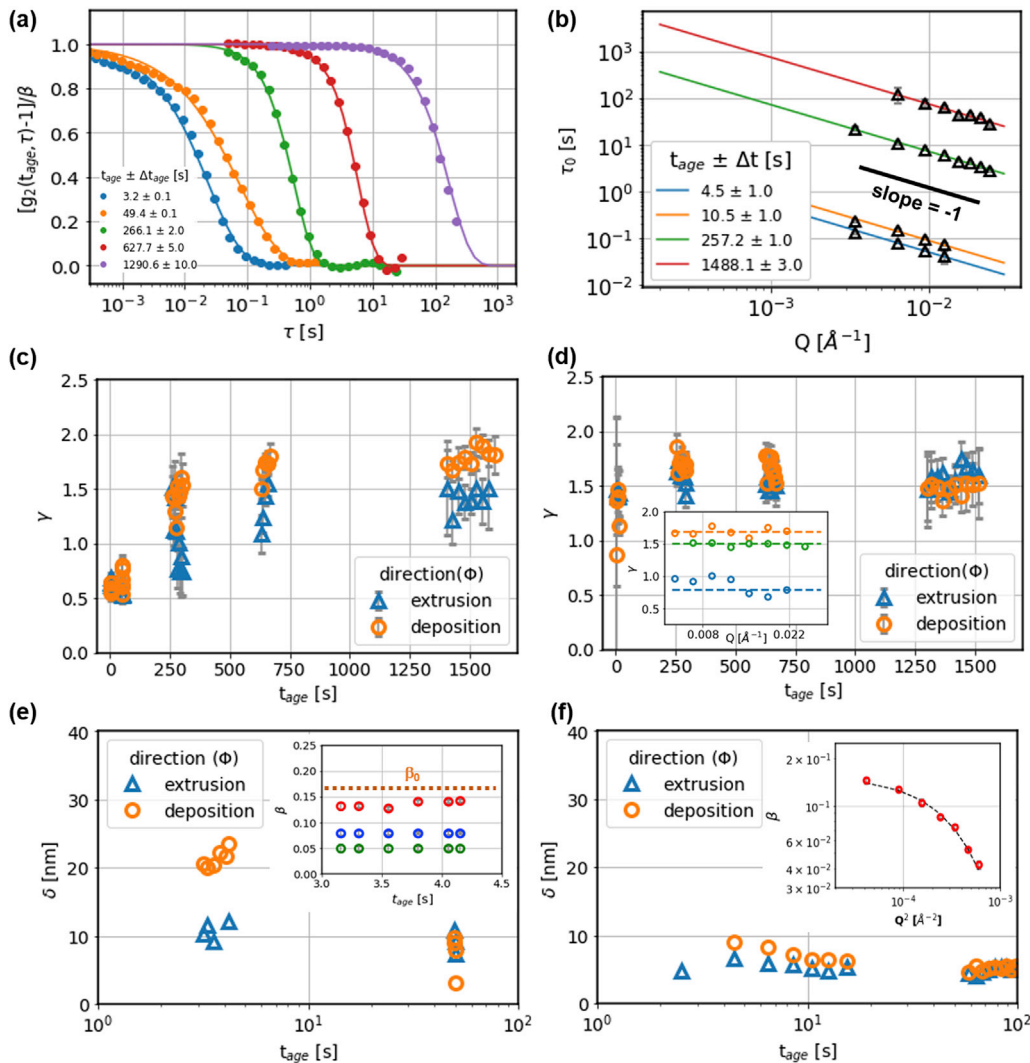
Fig. 2. (a) Normalized aged correlation functions for the mono SiO$_2$ ink on an uncoated Si wafer collected at h = 50 μm above the substrate, in the extrusion direction (normal to the substrate) and for a wavevector Q = 0.0064 Å^{-1}. (b) Overview of relaxation time τ_0 dependence on filament age t_{age} and wavevector Q, for the branched SiO$_2$ ink in the extrusion direction on the Crystalbond-coated substrate, slope indicates the drift velocity v_d. Time dependence of the compression exponent γ (averaged over Q), upon printing on Crystalbond substrates (c) mono SiO$_2$ and (d) branched SiO$_2$; inset: typical Q-dependence of the compression exponent γ in the subdiffusive (bottom, uncoated substrate along extrusion direction, t_{age} = 6.5 s) and hyperdiffusive regimes (middle, uncoated substrate along extrusion direction, t_{age} = 109 s, top: hydrophobic substrate along deposition direction, t_{age} = 1488 s). Mean square displacement δ of the colloids' fast dynamic modes within the 'cages' formed by their nearest neighbors: (e) Mono SiO$_2$, uncoated substrate; inset: Q-dependence of β at early ages for Q = 0.0094, 0.0064, 0.0034 Å^{-1} (bottom to top), dashed line is the contrast β_0 measured with a static reference sample. (f) Branched SiO$_2$, uncoated substrate; inset: Q-dependence of β for t_{age} = 6.5 s, dashed line is a fit to the relation β ∝ exp(-Q^{2}δ^2/3).

accessible in the experiment. For both ink systems, these fast localized dynamics show now no dependence on the substrate coatings.

While Brownian motion exhibits a dispersion $\tau_0 \propto Q^{-2}$, the investigated systems display a linear Q-dependence, as is typical for concentrated systems with highly interacting colloids [50,51]. This behavior indicates that the particle displacement, on average, increases linearly with time [41]. The dynamics is therefore not governed by diffusive motion but rather by a drift mechanism, with a drift velocity v_d [52] which is given as follows:

$$\tau_0\left(t_{age}, \Phi\right) = v_d^{-1}\left(t_{age}, \Phi\right) \cdot Q^{-1} \qquad (5)$$

Fig. 2b shows representative fits to Eq. (5) for the relaxation times determined for the branched SiO$_2$ ink in the extrusion direction for different ages. The drift velocity v_d is observed to shift toward lower mobility values as time progresses after printing. A

complete overview of the evolution of v_d for both investigated inks and printing directions (Φ) is presented in Fig. 3.

The displacement velocity v_d can be expected to depend on Φ, where the differences between the analyzed directions (extrusion versus deposition) arise from the process inherent anisotropies (shear distribution during extrusion and deformation upon deposition) and the contribution of the substrate interactions. Summary plots of the time-dependent v_d for the ink systems printed on the different substrates are presented in Fig. 3a–d. Here, v_d represents the mobility of the system and therefore the ability for mass transport and interaction with the surroundings. It is therefore pertinent to emphasize the probing location for this investigation — on the printed filaments ≈50 μm above the substrate. At early stages (right after deposition), the values for v_d are maximum: the system is far from equilibrium and the colloidal particles (and other ink molecules) are rapidly changing their configuration as a result of the shear-stress applied during the extrusion, and the 90°
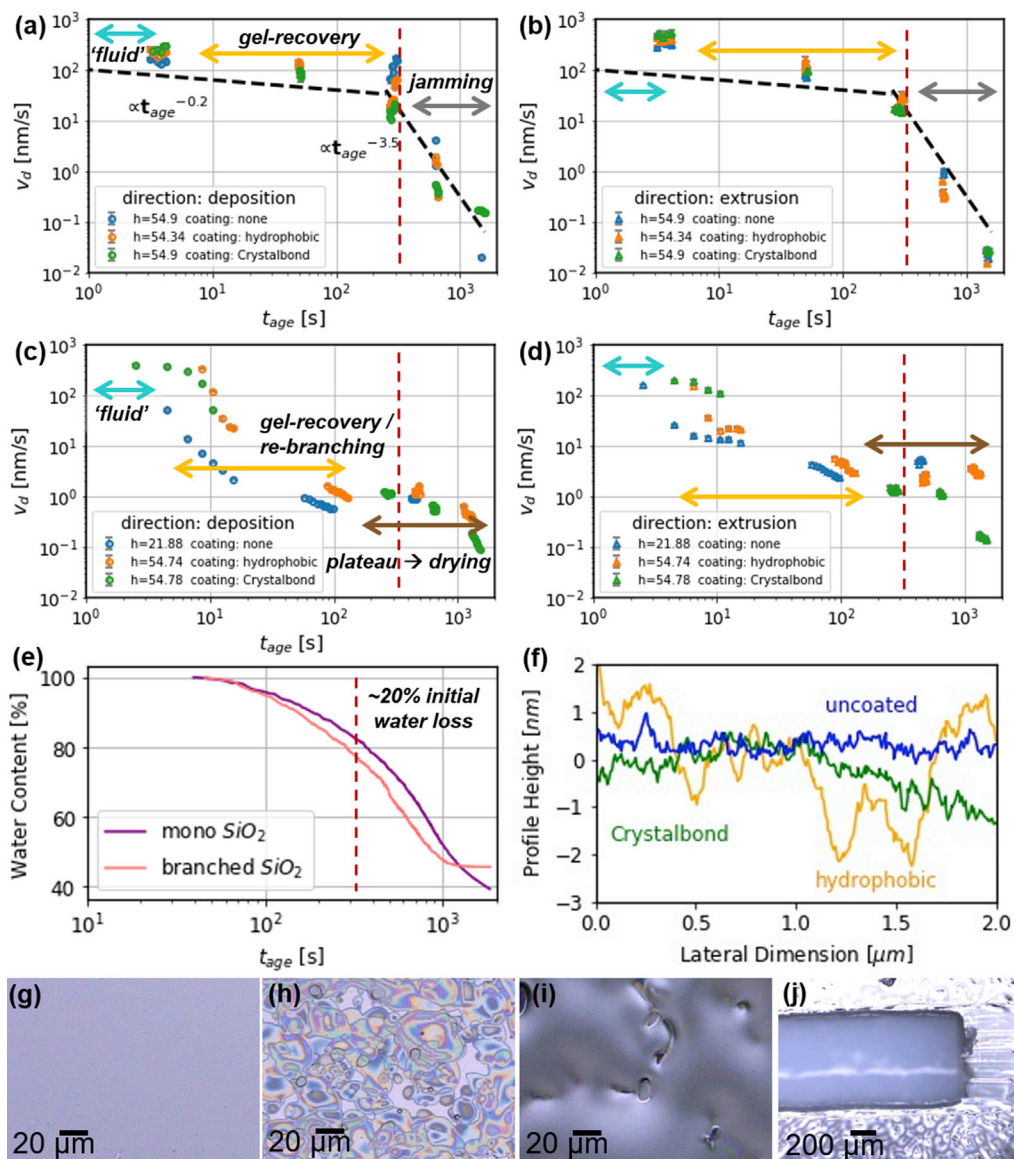
Fig. 3. Drift velocity v_d for the investigated inks upon filament deposition on various substrates (a and b) monodisperse ink (mono SiO_2) and (c and d) branched SiO_2, in the deposition (a) and (c) and extrusion (b) and (d) directions. Arrows (from left to right) indicate the ink relaxation stages as 'fluid', gel recovery and jamming (a and b, for mono SiO_2) and 'fluid', gel recovery/rebranching and plateau drying (c and d, branched SiO_2). (e) Room temperature thermogravimetric analysis of extruded inks showing the solvent (water) evaporation. Dashed vertical lines in (a–e) indicate an approximate water loss of 20% at $t_{age} \approx 300$ s. (f) AFM surface profile; and optical microscopy images of the substrates (g) uncoated Si wafer, (h) hydrophobic Si-coating, and (i) Crystalbond coating. (j) Printed structure from the branched SiO_2 ink on the Crystalbond-coated substrate, with a sliding path at the end of the structure. AFM, atomic force microscopy.

deformation induced by the substrate and the relative motion of the nozzle to the substrate [53]. After the deposition, the mobility of the systems decreases as a result of the ink relaxation (settling, recovery of the gel structure) and the evaporation of solvent (drying, Fig. 3e). While the mobility decreases for both the extrusion and deposition directions, slightly larger values are observed in the extrusion direction. This result is associated with the 'pinning' that the ink experiences near the ink-substrate interface, restricting the motion along the deposition direction. In contrast, the mobility along the extrusion direction is not as greatly affected by the pinning effect but is instead dominated by bulk phenomena such as gel structure recovery and solvent evaporation, which locally increases the viscosity. The effects of the latter can be better observed at later ages and eventually reduce the mobility along both directions and drive the system toward a jammed state.

The evolutionary pathways for v_d differ depending on the colloid structure (i.e. monodisperse vs. branched), which highlights the significance of the materials' contribution to the out-of-equilibrium stages associated with the AM processing. For the mono SiO_2 system, v_d decreases slowly for ages 3 s > t_{age} > 300 s. The observed large spread of v_d at $t_{age} \approx 300$ s, in particular in the deposition direction, stems from the occurrence of dynamic heterogeneities as discussed in section 3.2. For t_{age} > 300 s, v_d decreases at a significantly higher rate for all substrates and along both directions. The dependence of v_d on t_{age} can in both regimes be approximated by power laws, that is, $v_d \propto t_{age}^m$. Guides to the eye with m = −0.2 for t_{age} < 300 s and m = −3.5 for t_{age} > 300 s are shown in Fig. 3a, b. The transition around 300 s can be linked to the loss in solvent, as suggested by the room temperature TGA analysis, where the change in water content is about 20% (Fig. 3e) for the

corresponding t_{age} (the other solvents in the inks have significantly higher vapor pressures at room temperature). For these TGA measurements, extruded filaments with comparable dimensions where subjected to constant temperature programs reproducing the XPCS environmental conditions. TGA and dynamics measurements suggest that water loss at 20% drives the mono SiO_2 ink systems into jamming, accompanied by a rapid loss in colloid mobility. Consequently, one may characterize the initial state of the ink right after deposition as 'fluid-like', characterized by fast, sub-diffusive dynamics and the presence of fast dynamic modes. This is followed by a phase in which it recovers and strengthens its gel structure, until jamming and solidification sets in driven by solvent evaporation.

Compared with the two power law regimes, the branched SiO_2 ink system exhibits a more complex v_d (t_{age}) evolution, refer Fig. 3c, d. The initial 'fluid-like' phase right after deposition is followed by a steep decrease in v_d for $t_{age} < 20$ s. We hypothesize that this regime is governed by the recovery of the gel structure and (re-)branching of the colloidal particles. This decrease of v_d sets in at significantly earlier ages on the bare substrate, as compared with the hydrophobic and Crystalbond-coated cases, respectively, pointing toward a possible pinning or bonding with the uncoated substrate. For 400 s > t_{age} > 60 s, v_d is almost independent of t_{age}, with v_d showing only small variation for the different substrate coatings. This plateau region may be attributed to a steady state in which branches with neighboring colloids have formed, and the overall mobility is determined by the amount of solvent (or in return the packing density of the colloidal particles) in the system. The final decrease in v_d can be associated with the solvent evaporation and drying as evidenced from the room temperature TGA in Fig. 3e. Given the lower initial colloidal volume fraction in the branched SiO_2 ink (when compared to the mono SiO_2 formulation, refer Table 1), it may be expected to find the onset of drying in the dynamics at larger t_{age}, when a similar particle volume fraction is met upon further solvent removal.

The colloid mobility as characterized by v_d is also observed to exhibit variations depending on the substrate properties, indicating overall lower mobility right after deposition and up to ~100 s when printing on uncoated silica substrates. For the branched SiO_2 ink system, it should be noted however that data were acquired at ~20 μm from the substrate interface, which emphasizes the pinning promoted by the substrate surface, at short aging times in comparison with the hydrophobic and Crystalbond counterpart samples probed at ~50 μm. These findings may be related to the properties governing the ink-substrate interaction, including substrate wetting, surface chemistry, and mechanical properties of the coating. In particular, the work of adhesion W_a (calculation details in Supplementary Information Section S1.) of the respective inks' solvent mixtures is largest for the uncoated substrates, followed by the Crystalbond and the hydrophobic coated surfaces, refer Table 2. It should be noted that these values are a fair approximation [54] to the actual inks W_a at the earlier ages after deposition, when the inks solvent content is maximum.

In the case of the branched SiO_2 ink, very small variations in v_d were observed between the hydrophobic and Crystalbond coatings (Fig. 3c, d), presumably owing to the poor wetting properties of the former [31] and the plasticity of the latter. Differences become significant at later ages where the hydrophobic coating shows higher v_d values in both analyzed directions. The substrates' surface morphologies can be appreciated in Fig. 3g-j; a trench-like mark on the Crystalbond coating can be observed (Fig. 3j), as it deformed upon volumetric contraction of the above-laying filament along the deposition direction. The ability for the filament to 'flow' during drying is most pronounced for the Crystalbond coating and should allow for a partial release of the stress induced by the volumetric contraction. Similarly, for the mono SiO_2 ink system, the highest v_d values were obtained when printing on Crystalbond-coated substrates. This is especially significant at later stages, where the difference between v_d for Crystalbond and uncoated substrates span over one order of magnitude along the deposition direction.

The surface AFM characterization (Fig. 3f) indicates the roughness to be fairly similar despite the differences observed in the 'waviness' of the height profiles, refer Fig. 3f-i. The roughness values are largest for the hydrophobic system, followed by the Crystalbond coating and the uncoated substrates. This result in connection with the measured contact angle and roughness factors, accounts for the relatively poor wetting properties of the inks on the hydrophobic coating and increasingly better wetting on the Crystalbond and uncoated surfaces, respectively. Refer Tables 2 and 3.

3.2. Dynamic heterogeneities

The two ink systems, in which the filler particles are packed at high volume fraction, have a dynamical behavior (for ages past the initial gel recovery) that are reminiscent of that of colloidal gels. Typical dynamics in such systems are characterized by slow relaxations, non-exponential, ballistic-like correlation functions, and non-diffusive ($\tau_0 \propto Q^{-1}$) behavior [55–60]. In this age regime, the systems are being driven into a jammed and arrested state by solvent evaporation and the accompanying volume shrinkage. The dynamics of these systems can be expected to be temporally heterogeneous and driven by stress relaxation processes [44]. The temporal heterogeneities can be quantified by means of the normalized variance χ (Eq. (4)). χ is calculated for data sets with $t_{age} > 200$ s, where the timescales of the dynamics, as characterized by g_2, are quasi-static over an extended range of ages, allowing for the calculation of χ with decent statistics, while avoiding artifacts due to changing relaxation times τ_0. While the dynamics of the branched SiO_2 ink shows no significant temporal heterogeneities within the range of ages investigated here, such heterogeneities are very pronounced in the monodisperse ink system and show a clear dependence on the substrate coating.

Fig. 4a, b show the $\chi(Q, \Phi, t_{age}, \tau)$ calculated for the mono SiO_2 ink on the three different substrates for the deposition and extrusion directions at three different ages and for $Q = 0.00642$ Å^{-1},

Table 2
Inks' solvent mixtures wetting characteristics on the different substrates.

Solvent mixture	Surface Energy (liquid) γ_L [mJ/m^2]	Coating	Contact angle θ_c [°]	W_a [mJ/m^2]
Mono SiO_2	70.71	Uncoated	44.80	120.88
		Hydrophobic	89.65	71.14
		Crystalbond	63.79	101.94
Branched SiO_2	51.71	Uncoated	33.81	94.68
		Hydrophobic	74.26	65.74
		Crystalbond	43.23	89.39

Table 3
Substrate properties characterized by AFM and sessile drop contact angle measurements.

Coating	Roughness R_q(RMS) [nm]	Roughness factor φ_r	Surface energy (substrate) γ_S [mJ/m^2]
Uncoated	2.29426	1.00161	61.64
Hydrophobic	3.94313	1.00099	19.31
Crystalbond	2.43718	1.00126	38.36

AFM, atomic force microscopy.
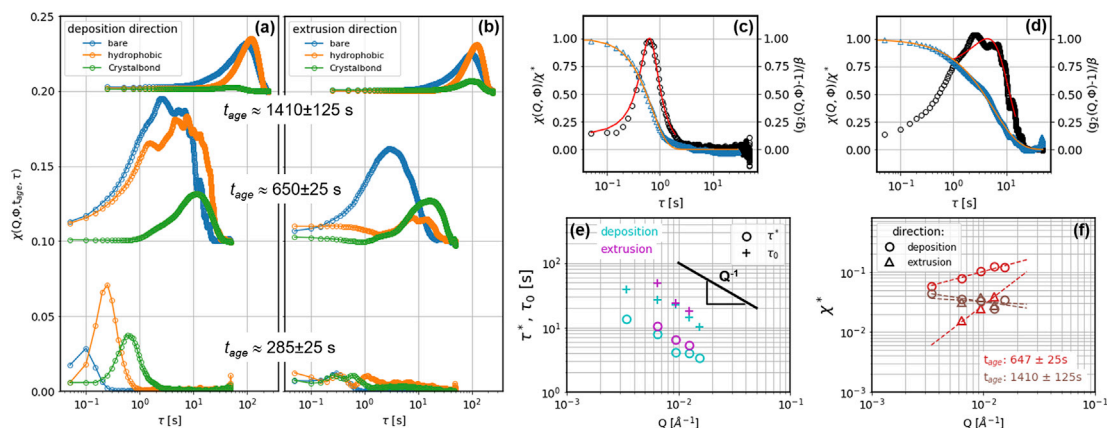
Fig. 4. Normalized variance χ for the mono SiO$_2$ ink on differently coated substrates along the deposition (a) and extrusion (b) directions, at three different ages (data sets for $t_{age} \approx 650$ s and $t_{age} \approx 1410$ s are shifted along the y-axis by 0.1 and 0.2, respectively). Comparison of χ and g2 for (c) the Crystalbond substrate at $t_{age} = 284 \pm 25$ s and (d) bare substrate at $t_{age} = 650 \pm 25$ s. The fit of g2 uses Eq. (3), while χ is fitted with an asymmetric pseudo-Voigt profile. (e) Comparison and Q-scaling of the g2 correlation time τ_0 and the characteristic timescale τ^* of the dynamic heterogeneities for the ink at $t_{age} = 647 \pm 25$ s on the hydrophobic substrate. (f) Q-scaling of χ^* for different ages on the hydrophobic substrate. Dashed lines are fits according to $\chi^* \propto Q^\alpha$.

corresponding to a length scale of about 100 nm, comparable with the colloid radius. The average ages span the onset of the 'aging regime' ($v_d \propto t_{age}^{-3.5}$) till the end of the time window observed in this study. The peak shape of χ provides insights about the timescales of the heterogeneities [44,61]. Depending on the substrate and relaxation regime, temporal heterogeneities with characteristic timescales τ^*, corresponding to the value of τ at the peak value χ^* of χ, develop. For $t_{age} \approx 650$ s, the χ calculated along the deposition direction for the bare and hydrophobic substrates exhibit some spikes, which are reminiscent of single events causing substantial decorrelations. For filaments on the uncoated substrate, with the highest chemical affinity (printing Si-based inks on Si wafers, which exhibit the best wetting properties, i.e. lowest contact angles, refer Table 2), the heterogeneities exhibit shorter timescales τ^* and are more pronounced (larger χ^*) than for the filaments on the other two substrates. For the Crystalbond coating, the ability of the filaments to 'flow' during volumetric contraction facilitates the accommodation of deformations near the ink/substrate interface. Consequently, the heterogeneities show larger characteristic times and lower maxima, suggesting that the local structure rearrangements occur more slowly and concomitantly, allowing for better stress distribution and potentially resulting in less large-scale structural defects. These results provide additional insights applicable to printing, for example, devices such as electronics, where good interfacial contact and conformity might be essential for electrical conductivity and signal transmission.

Previously reported mechanical properties for the hydrophobic coating indicate hardness values of ≈ 1.3 GPa, as measured by automated nanoindentation with a conical diamond probe, compared with reference hardness values for glass slides with values of ≈ 7.5 GPa [32]. For Crystalbond 509, on the other hand, no hardness values were found on literature, instead temperature-dependent viscosity was reported, which confirms our

observations on the ability of this coating to 'flow'. With a melting temperature of 74 °C, the reported viscosity is 26000 cP [62]. Nevertheless, at the temperatures used for printing at ≈ 25 °C, this material behaves as a solid. The emergence of dynamic heterogeneities is correlated both with the work of adhesion W_a between the ink and the substrate and the mechanical properties of the substrate. Temporal heterogeneities in the dynamics stem from stress relaxation during volumetric shrinkage (upon solvent evaporation) and are augmented by 'pinning' effects between the ink and the substrate. This 'pinning' raises the energy barrier for structural rearrangements, reducing the frequency of these rearrangement events, while at the same time increasing their average amplitude in terms of structural displacement. Careful optimization of W_a and the mechanical properties of the substrate may minimize resulting defects such as cracks and voids in the final structure.

The dynamic heterogeneities are generally more pronounced in the writing direction than in the extrusion direction. This result may be expected, since the substrate interface provides anchoring sites for the ink to adhere. In the extrusion direction, on the other hand, the ink is not only less constricted to motion but also more likely to accept solvent species from the bulk, on their pathway toward the filaments' periphery where its exchange with the surroundings is maximum. This observation agrees with v_d showing larger values in the extrusion direction for $t_{age} > 1000$ s.

Fig. 4c, d show a quantitative comparison of the timescales τ_0 of the one-time correlation function g2 and the characteristic time τ^* of the dynamic heterogeneities. Here, τ^* is determined as the position of the maximum χ^* of a fit of χ with an asymmetric pseudo-Voigt profile [63], which averages out some of the spikes in χ. For all data sets, τ_0 is found to be larger than τ^* by about a factor 3 to 4, indicative of fast non-gaussian processes that are characteristic of jammed systems [61]. Taking into account that the g2s are strongly compressed ($\gamma \geq 1.5$) and comparing τ^* to the τ corresponding to

the 'half-height' of g_2 instead, this factor is reduced to about 2. In general, for glassy systems such as concentrated colloidal suspensions, τ^* is of the same order of magnitude and proportional to τ_0 [39,42,43]. An example of the scaling of τ^* and τ_0 with Q for the mono SiO_2 ink on the hydrophobic substrate at $t_{age} \approx 250$ s is shown in Fig. 4e, confirming this universal scaling relationship in both analyzed directions. An example of the scaling of χ^* with Q is shown in Fig. 4f for $t_{age} \approx 650$ s and $t_{age} \approx 1410$ s for a filament printed on the hydrophobic substrate. For $t_{age} \approx 250$ s, the accessible Q range was too limited to reliably determine the Q-dependence. For $t_{age} \approx 650$ s, $\chi^* \propto Q^\alpha$ with α ranging from 0.12 ± 0.04 to 1.77 ± 0.65, thus $\alpha > 0$ for the bare and hydrophobic substrates, while $\alpha \approx -0.1$ for the Crystalbond-coated substrate. For $t_{age} \approx 1410$ s, $\alpha < 0$ for all substrates with $-0.11 > \alpha > -0.3$. It has been reported that for colloidal gels χ^* may exhibit a non-monotonic behavior with Q, with a maximum at Q^* corresponding to the particle size or interparticle bond [42]. In our case, the particle-particle spacing (refer to section 3.3) in the mono SiO_2 ink corresponds to $Q \approx 0.0025$ Å^{-1}. Thus, the Q range over which χ^* is evaluated is close to the presumed peak position and one can generally expect a weak Q-dependence, with α transitioning from positive to negative values as Q increases. However, here the observed transition in α is related to t_{age} but within the same Q-range. Therefore, this transition cannot simply stem from a change in particle-particle distance and thereby a shift of Q^*, as the particle-particle distance is almost constant for $t_{age} > 600$ s (section 3.3), but rather points to subtle changes in the dynamic heterogeneities. Trappe et al [42] proposed a simple and generic scaling argument for the Q-dependence of dynamical fluctuations in glassy systems. The model is based on the assumption that the fluctuations in the dynamic correlations stem from fluctuations of N_{tot}, the total number of events needed to decorrelate the scattered X-rays, where $N_{tot} \propto N_{blob}N_{ev}$ with N_{blob} being the number of correlated regions ('blobs') within the scattering volume and N_{ev} the number of events that decorrelate the scattering on the timescale of the

system's relaxation. While there is no theory for the detailed scaling of N_{blob} and N_{ev} with Q and the solution might not be unique, a possible explanation for the observed transition in α involves an increase in the number of correlated regions N_{blob}, which is tantamount to a decrease in the average volume of the correlated regions (supplementary information, Fig. S4). The underlying mechanism might be the formation of microcracks and other defects, which are indeed detected for this ink system using X-ray nanotomography (section 3.4).

3.3. In situ structural analysis: SAXS

The XPCS data sets contain, in addition to the information about the dynamics, time-resolved SAXS data, which are used to obtain structural information during the inks' deposition, relaxation, and drying processes. Contrary to the dynamics, no anisotropy (Φ-dependence) could be detected in a quantitative analysis of the SAXS patterns.

The mean particle distance, as defined by $2\pi\sqrt{3/2}/Q_c^{<111>}$, $Q_c^{<111>}$ being the center position of the <111> reflection, (Fig. 5a), exhibits a distinct drop for 300 s $< t_{age} < 600$ s that corresponds to the accelerated power-law gel recovery stage observed for the mono SiO_2 ink system and is attributable to volumetric shrinkage as suggested by the TGA result (Fig. 3e). At the same time, the average domain size (Fig. 5b), defined by $2\pi/Q_{FWHM}^{<111>}$, where $Q_{FWHM}^{<111>}$ is the FWHM of the <111> reflection, increases by about 250 nm. This size increase corresponds well to the mean particle distance and shows that the domains in this ink grow slightly as the overall volume decrease takes place.

For the mono SiO_2 ink system, the form factor $P(Q)$ of the spherical colloids, measured from a diluted suspension (1 vol% in water) and fitted to the form factor for spherical particles [64], reveals a colloid diameter of 237.4 ± 0.3 nm with a polydispersity of about 2% (Fig. S5. supplementary information). The age-dependent structure factor $S(Q,t_{age})$ is determined by dividing the measured
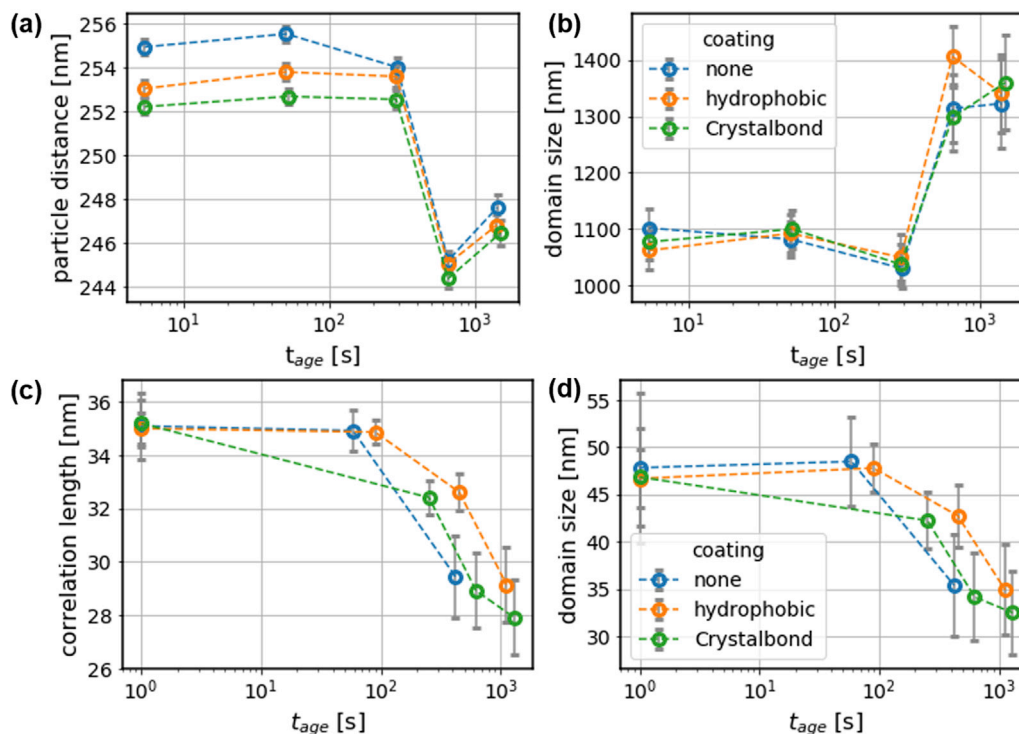

Fig. 5. (a) Interparticle distance and (b) domain size, for mono SiO_2 ink; (c) correlation length and (d) domain size, for branched SiO_2 ink, extracted from the time-resolved SAXS analysis during printing. Dashed lines are a guide to the eye. SAXS, small angle X-ray scattering.

and radially averaged SAXS intensity I(Q, t_{age}) by P(Q,t_{age}), where P(Q,t_{age}) is the previously determined form factor corrected by an age-dependent background arising from the changing electron density in the solvent mixture due to the evaporation of water with time. The identified structure factor peaks follow approximate ratios of $Q/Q_1 = 1 : \sqrt{4/3} : \sqrt{8/3}$ (supplementary information), indicative of the nearly monodisperse spheres being packed into a face-centered cubic (FCC) arrangement. A noticeable shift in peak positions toward larger Q with increasing t_{age} indicates that the lattice parameter of the FCC packing is getting smaller as water evaporates from the ink after deposition, as shown in Fig. S5b. in supplementary information.

In contrast, for the branched SiO_2 ink system, the large polydispersity of the fumed silica aggregates suppresses distinct form factor oscillations even in a dilute (1 vol%) suspension. For this corresponding ink system, only a broad structure factor peak can be observed in the I(Q). Contrary to the monodisperse case, there are little changes in the observable features as solvent evaporates, and hence the structure factor was determined as S(Q,t_{age}) = I(Q,t_{age})/ I_{dilute}(Q). The correlation length ($2\pi/Q_c$) and domain size ($2\pi/Q_c^{FWHM}$) obtained by fitting S(Q,t_{age}) to a pseudo-Voigt function are shown in Fig. 5c, d, respectively, where Q_c is the center of the pseudo-Voigt and Q_c^{FWHM} its FWHM. Despite the formation of branches between silica aggregates, this ink does not develop a structural order beyond an average nearest neighbor distance. As for mono SiO_2, the correlation length and domain size change noticeable for 300 s < t_{age} < 600 s, corresponding to a loss of $\approx 20\%$ in the ink's water content according to the TGA (Fig. 3e). With the correlation length decreasing by about 20%, the domain size also increases by about 30%.

Thus, the two inks exhibit a very different structural evolution: the mono SiO_2 ink only slightly increases its packing density, while growing the average domain size during solvent evaporation, increasing the energy barriers for the required larger scale structural rearrangements. In contrast, the branched SiO_2 ink significantly increases its packing density, starting from a lower volume concentration than that of the mono SiO_2 ink, while its already poor ordering further decreases. Moreover, despite its branching nature, the branched SiO_2 ink displays a much more 'fluid' behavior, that is, branches are broken and reformed easily to accommodate volume shrinkage, in accordance with the breaking and reformation of branches under modest shear observed in the dynamics during extrusion and deposition.

Contrary to the dynamics, the average structural evolution of the two ink systems, as probed by SAXS, only shows little variation with substrate coating, indicating that the observed behavior is dominated by the characteristics of the bulk material. Nevertheless, a direct correlation can be established regarding the mechanical properties of the coatings and their chemical affinity with the inks. It is observed that those substrates with higher chemical affinity (uncoated) and with higher elastic moduli (i.e. harder materials, namely uncoated and hydrophobic coated) present higher resistance to the inks (colloid) motion, in turn exhibiting higher nearest-neighbor distances for a given age time. In contrast, the Crystalbond-coated substrates being a highly mobile resin-like material exhibit the least resistance to microstructural rearrangements (for both ink systems). This result is tightly related to the wetting properties of the inks' solvent mixtures, where the largest work of adhesion W_a is measured for the uncoated and the smallest for the hydrophobic-coated substrates.

3.4. Ex situ structural analysis: electron and X-ray microscopy

The original structural characteristics of the colloids (i.e. branched vs monodisperse, primary particle and aggregate size) strongly influence the printed filaments' mesostructure evolution and defect formation as noted from the time-resolved SAXS results. Moreover, after annealing the structures at 700 °C for 20 min, the filaments' cross-sections on the uncoated substrates (see low magnification electron microscopy images, Fig. 6a, d) exhibit signs of strong pinning to the substrate, volumetric contraction, and, in the case of the mono SiO_2 ink system, macroscale dislocations. The
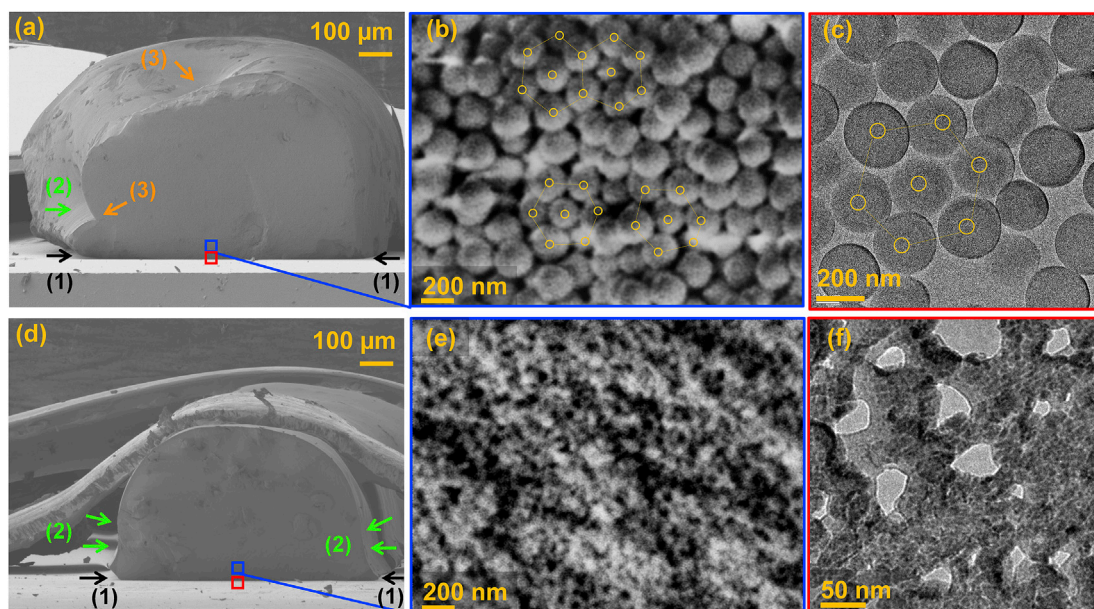

Fig. 6. *Ex situ* electron microscopy characterization of printed structures on uncoated substrates after annealing at 700 °C for 20 min, from inks with monodisperse colloids (mono SiO_2 ink) (a–c) and branched colloids (branched SiO_2 ink) (d–f). Arrows in (a) and (d) indicate (1) pinning to the substrate, (2) volumetric contraction, and (3) macroscale dislocations. 'Rope'-like structures observed around the printed filament in (d) correspond to conductive Cu-tape used to improve the evacuation of electric charges that accumulate in dielectric materials such as SiO_2 during SEM observation. SEM images (b) and (e) show the self-assembled cross-section at ~ 50 μm from the ink/substrate interface. TEM images (c) and (f) correspond to cross-sections at ~1–5 μm from the ink-substrate interface. SEM, scanning electron microscopy. TEM, transmission electron microscopy.

latter are likely to have occurred during the later jamming transition ($t_{age} > 300$ s), where the strong temporal heterogeneities were observed accompanied by significant solvent evaporation, causing the colloids to come into close contact and the relaxation behavior to be dominated by dynamic heterogeneities. In addition, in images (c) and (f), the final colloidal assembly shows different packing patterns, where the monodisperse colloids exhibit a closed packing (resembling hexagonal lattice arrangements), and the branched colloids form a porous interconnected structure. In the case of the mono SiO_2 ink system, these observations can be readily correlated with the SAXS results that indicate the nearest neighbor distance decreases at around 600 s, while at the same time the domain size increases from about four to five colloid units. Keeping in mind that the heat treatments may affect the colloidal mesoscale assembly, a

structure containing domains of five colloidal units with a mean interparticle distance of about one colloid diameter can only be found when the close packed configuration is attained. Such mesoscale structure, formed during the postdeposition stages of the ink's relaxation, will therefore serve as the 'seed' assembly patterns of the materials microstructure and dictate their hierarchical ordering and complexity.

X-ray nanotomography analysis of both mono SiO_2 and branched SiO_2 filaments annealed at 700 °C for 20 min are shown in Fig. 7. These specimens have been prepared from the central region of the filament next to the substrate interface using FIB (section 2.3). As shown in the Fig. 7a, a large crack (highlighted in yellow) exists in the mono SiO_2 sample. Colloids are colored in blue. The large crack runs through the cropped region transversely, parallel
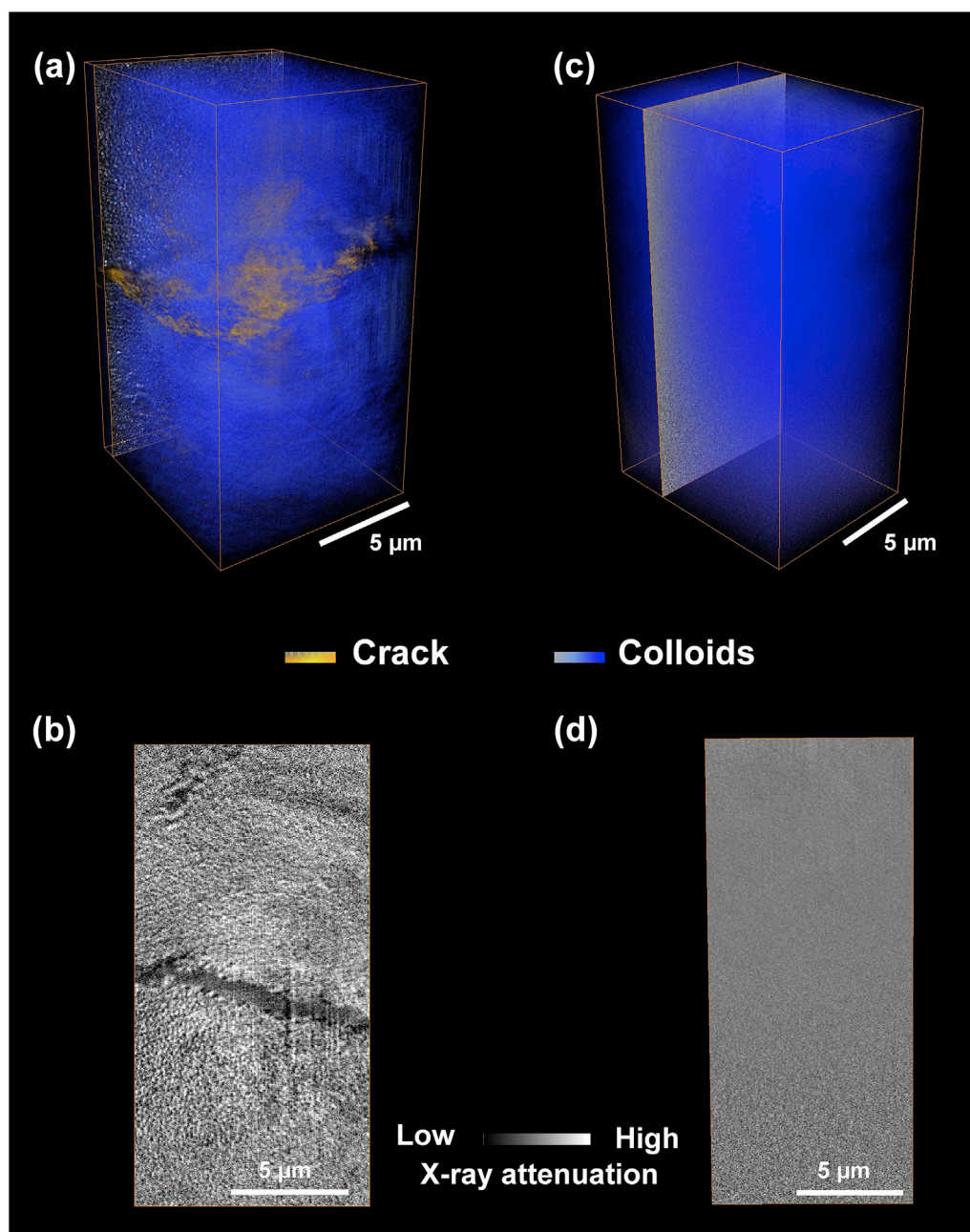

Fig. 7. X-ray nanotomography characterization of printed structures after annealing at 700 °C for 20 min, from monodisperse colloids by (a) 3D volume visualization and (b) pseudo cross-section view and branching colloids by (c) 3D volume visualization and (d) pseudo cross-section view.

to the deposition direction and to the substrate. There are also a few smaller cracks distributed along the vertical direction. These can be better visualized from pseudo cross-section images as shown in Fig. 7b, represented by a darker gray color. The length of the smaller cracks is ~5 μm. The color in the pseudo cross-section images represents the different X-ray attenuation levels (higher attenuation corresponding to lighter shades of gray). In contrast, no obvious cracks were observed in the specimen from branched SiO_2 inks. This important difference can be attributed to the intrinsic aggregating character of the branched colloids that form a strong interconnected network (as observed from the transmission electron microscopy (TEM) images), in addition to their smaller primary and aggregate particle size, which may result in more favorable conditions for neighboring particle to coalesce. In addition, the FCC colloidal assembly in the mono SiO_2 ink potentially favors the propagation of cracks along high-density planes. The specimens used for the X-ray nanotomography are representative samples in the sense that they were prepared from the same filaments deposited during the X-ray experiments and intersect the X-ray scattering volume in the bulk of the material. Therefore, they do not highlight any surface effects that would in turn only contribute marginally to the X-ray scattering signal. Because the total filament volume sampled by X-ray nanotomography is relatively small, it provides qualitative, complimentary information to the X-ray scattering results, rather than providing a quantitative measure of the defects.

4. Conclusions

The out-of-equilibrium stages associated with 3D printing of viscoelastic colloidal inks were investigated *in operando* by XPCS, revealing the effects of colloidal structure and substrate properties on the inks' mesoscale relaxation processes and structural evolution near the substrate interface. The bulk properties of the inks, their interactions with substrates, and the ability of the substrate to accommodate deformations of the deposited filaments determine the solidification kinetics of the inks and their final nanoscale and mesoscale structure. Signatures in the relaxation dynamics, such as the occurrence of temporal heterogeneities, can be related to volumetric shrinkage and defect formation by *in situ* and *ex situ* structural analysis.

Our study is aimed at bridging physics and material science, using state-of-the art X-ray scattering techniques to reveal underlying colloid physics in CDW under out-of-equilibrium processing conditions. Detailed information about the structural and dynamical mesoscale evolution can be extracted from the same time-resolved coherent scattering data set, making this technique a good match for this kind of *operando/in situ* studies. Such an understanding of the evolution of nanocomposites at length scales and timescales corresponding to nanoparticle size and dynamics may inform multiscale physics simulations of materials such as colloidal inks under processing conditions. While the present study is focused on the ink-substrate interactions, one can expect similar findings for filament-filament interfaces in 3D printed multilayer structures, where the properties of the 'substrate', that is, the lower filament, will be age dependent.

Credit author statement

Maria Torres Arango: Conceptualization, Methodology, Investigation, Formal Analysis, Visualization, Writing, Editing; **Yugang Zhang:** Software, Formal Analysis, Visualization, Data Curation; **Chonghang Zhao:** Investigation, Formal Analysis, Visualization **Ruipeng Li:** Editing, Supervision, Funding Acquisition; **Gregory Doerk:** Writing, Editing, Supervision, Funding Acquisition; **Dmytro**

Nykypanchuk: Investigation, Formal Analysis, Editing; **Yu-chen Karen Chen-Wiegart:** Formal Analysis, Validation, Data Curation, Writing, Supervision; **Andrei Fluerasu:** Formal Analysis, Validation, Supervision; **Lutz Wiegart:** Conceptualization, Investigation, Formal Analysis, Visualization, Validation, Data Curation, Software, Resources, Writing, Editing, Supervision, Funding Acquisition

Declaration of competing interest

The authors declare no conflicts of interest related to this work.

Appendix A. Supplementary data

Supplementary data to this article can be found online at https://doi.org/10.1016/j.mtphys.2020.100220.

References

[1] J.A. Lewis, J.E. Smay, J. Stuecker, J. Cesarano, Direct ink writing of three-dimensional ceramic structures, J. Am. Ceram. Soc. 89 (2006) 3599–3609, https://doi.org/10.1111/j.1551-2916.2006.01382.x.

[2] A.R. Studart, Additive manufacturing of biologically-inspired materials, Chem. Soc. Rev. 45 (2016) 359–376, https://doi.org/10.1039/c5cs00836k.

[3] T.D. Ngo, A. Kashani, G. Imbalzano, K.T.Q. Nguyen, D. Hui, Additive manufacturing (3D printing): a review of materials, methods, applications and challenges, Compos. B Eng. 143 (2018) 172–196, https://doi.org/10.1016/j.compositesb.2018.02.012.

[4] J.R. Raney, J.A. Lewis, Printing mesoscale architectures, MRS Bull. 40 (2015) 943–950, https://doi.org/10.1557/mrs.2015.235.

[5] I. Gibson, D. Rosen, B. Stucker, Additive Manufacturing Technologies, 2015, https://doi.org/10.1007/978-1-4939-2113-3.

[6] A. Zhakeyev, P. Wang, L. Zhang, W. Shu, H. Wang, J. Xuan, Additive manufacturing: unlocking the evolution of energy materials, Adv. Sci. 4 (2017), https://doi.org/10.1093/nar/13.18.6559.

[7] K. Sun, T.-S. Wei, B.Y. Ahn, J.Y. Seo, S.J. Dillon, J.A. Lewis, 3D printing of interdigitated Li-ion microbattery architectures, Adv. Mater. 25 (2013) 4539–4543, https://doi.org/10.1002/adma.201301036.

[8] Y.L. Kong, I.A. Tamargo, H. Kim, B.N. Johnson, M.K. Gupta, T.-W. Koh, H.-A. Chin, D.A. Steingart, B.P. Rand, M.C. McAlpine, 3D printed quantum dot light-emitting diodes, Nano Lett. 14 (2014) 7017–7023, https://doi.org/10.1021/nl5033292.

[9] Q. Fu, E. Saiz, A.P. Tomsia, Direct ink writing of highly porous and strong glass scaffolds for load-bearing bone defects repair and regeneration, Acta Biomater. 7 (2011) 3547–3554, https://doi.org/10.1016/j.actbio.2011.06.030.

[10] J.L. Simon, S. Michna, J.A. Lewis, E.D. Rekow, V.P. Thompson, J.E. Smay, A. Yampolsky, J.R. Parsons, J.L. Ricci, In vivo bone response to 3D periodic hydroxyapatite scaffolds assembled by direct ink writing, J. Biomed. Mater. Res. 83A (2007) 747–758, https://doi.org/10.1002/jbm.a.31329.

[11] M.A. Torres Arango, D. Kwakye-Ackah, S. Agarwal, R.K. Gupta, K.A. Sierros, Environmentally friendly engineering and three-dimensional printing of TiO 2 hierarchical mesoporous cellular architectures, ACS Sustain. Chem. Eng. 5 (2017) 10421–10429, https://doi.org/10.1021/acssuschemeng.7b02450.

[12] F. Mendez-Arriaga, E. de la Calleja, L. Ruiz-Huerta, A. Caballero-Ruiz, R. Almanza, TiO2 3D structures for environmental purposes by additive manufacturing: photoactivity test and reuse, Mater. Sci. Semicond. Process. 100 (2019) 35–41, https://doi.org/10.1016/j.mssp.2019.04.034.

[13] J. Cesarano, R. Segalman, P. Calvert, Robocasting provides moldless fabrication from slurry deposition, Ceram. Ind 148 (1998) 94–101. http://cat.inist.fr/?aModele=afficheN&cpsidt=10641890.

[14] G.V. Franks, C. Tallon, A.R. Studart, M.L. Sesso, S. Leo, Colloidal processing: enabling complex shaped ceramics with unique multiscale structures, J. Am. Ceram. Soc. 100 (2017) 458–490, https://doi.org/10.1111/jace.14705.

[15] H. Elsayed, A. Chmielarz, M. Potoczek, T. Fey, P. Colombo, Direct ink writing of three dimensional Ti2AlC porous structures, Addit. Manuf. 28 (2019) 365–372, https://doi.org/10.1016/j.addma.2019.05.018.

[16] M.A. Torres Arango, A.S. Valença de Andrade, D.T. Cipollone, L.O. Grant, D. Korakakis, K.A. Sierros, Robotic deposition of TiO 2 films on flexible substrates from hybrid inks: investigation of synthesis–processing–microstructure–photocatalytic relationships, ACS Appl. Mater. Interfaces 8 (2016) 24659–24670, https://doi.org/10.1021/acsami.6b05535.

[17] F. Putz, S. Scherer, M. Ober, R. Morak, O. Paris, N. Hüsing, 3D printing of hierarchical porous silica and α-quartz, Adv. Mater. Technol. 3 (2018) 3–7, https://doi.org/10.1002/admt.201800060.

[18] N.A. Dudukovic, L.L. Wong, D.T. Nguyen, J.F. Destino, T.D. Yee, F.J. Ryerson, T. Suratwala, E.B. Duoss, R. Dylla-Spears, Predicting nanoparticle suspension viscoelasticity for multimaterial 3D printing of silica–titania glass, ACS Appl. Nano Mater. 1 (2018), https://doi.org/10.1021/acsanm.8b00821 acsanm.8b00821.

[19] B.G. Compton, J.A. Lewis, 3D-printing of lightweight cellular composites, Adv. Mater. 26 (2014) 5930–5935, https://doi.org/10.1002/adma.201401804.

[20] K.J. Johnson, L. Wiegart, A.C. Abbott, E.B. Johnson, J.W. Baur, H. Koerner, Operando monitoring of dynamic recovery in 3D-printed thermoset nanocomposites by XPCS, Langmuir (2019), https://doi.org/10.1021/acs.langmuir.9b00766.

[21] M.A. Torres Arango, O.A. Abidakun, D. Korakakis, K.A. Sierros, Tuning the crystalline microstructure of Al-doped ZnO using direct ink writing, Flex. Print. Electron. 2 (2017): 035006, https://doi.org/10.1088/2058-8585/aa8801.

[22] M.A. Torres Arango, D.T. Cipollone, L.O. Grant, D. Korakakis, K.A. Sierros, Continuous-flow direct writing of hybrid TiO2 flexible photo-electrodes: processing, microstructure and functionality interrelations, MRS Adv. 2 (2017) 1021–1028, https://doi.org/10.1557/adv.2017.238.

[23] Y. Shmueli, Y.C. Lin, S. Lee, M. Zhernenkov, R. Tannenbaum, G. Marom, M.H. Rafailovich, In situ time-resolved X-ray scattering study of isotactic polypropylene in additive manufacturing, ACS Appl. Mater. Interfaces 11 (2019) 37112–37120, https://doi.org/10.1021/acsami.9b12908.

[24] A. Nogales, E. Gutiérrez-Fernández, M.C. García-Gutiérrez, T.A. Ezquerra, E. Rebollar, I. Šics, M. Malfois, S. Gaidukovs, K. Gē Cis, K. Celms, G. Bakradze, Structure development in polymers during fused filament fabrication (FFF): an in situ small- and wide-angle X-ray scattering study using synchrotron radiation, Macromolecules (2019), https://doi.org/10.1021/acs.macromol.9b01620.

[25] L. Wiegart, G.S. Doerk, M. Fukuto, S. Lee, R. Li, G. Marom, M.M. Noack, C.O. Osuji, M.H. Rafailovich, J.A. Sethian, Y. Shmueli, M. Torres Arango, K. Toth, K.G. Yager, R. Pindak, Instrumentation for in situ/ operando X-ray scattering studies of polymer additive manufacturing processes, Synchrotron Radiat. News 32 (2019) 20–27, https://doi.org/10.1080/08940886.2019.1582285.

[26] T.S. Arthur, D.J. Bates, N. Cirigliano, D.C. Johnson, P. Malati, J.M. Mosby, E. Perre, M.T. Rawls, A.L. Prieto, B. Dunn, Three-dimensional electrodes and battery architectures, MRS Bull. 36 (2011) 523–531, https://doi.org/10.1557/mrs.2011.156.

[27] I.J. Kramer, D. Zhitomirsky, J.D. Bass, P.M. Rice, T. Topuria, L. Krupp, S.M. Thon, A.H. Ip, R. Debnath, H.C. Kim, E.H. Sargent, Ordered nanopillar structured electrodes for depleted bulk heterojunction colloidal quantum dot solar cells, Adv. Mater. 24 (2012) 2315–2319, https://doi.org/10.1002/adma.201104832.

[28] M.H. Kumar, N. Yantara, S. Dharani, M. Graetzel, P.P. Boix, N. Mathews, Flexible, low-temperature, solution processed ZnO-based perovskite solid state solar cells, Chem. Commun. 49 (2013) 11089–11091, https://doi.org/10.1039/c3cc46534a.

[29] D. Liu, T.L. Kelly, Perovskite solar cells with a planar heterojunction structure prepared using room-temperature solution processing techniques, Nat. Photon. 8 (2014) 133–138, https://doi.org/10.1038/nphoton.2013.342.

[30] A.J. Kessman, D.R. Cairns, Template-assisted encapsulation of fluorinated silanes in silica films for sustained hydrophobic-oleophobic functionality, J. Colloid Interface Sci. 360 (2011) 785–792, https://doi.org/10.1016/j.jcis.2011.05.026.

[31] D.A. Banerjee, A.J. Kessman, D.R. Cairns, K.A. Sierros, Tribology of silica nanoparticle-reinforced, hydrophobic sol–gel composite coatings, Surf. Coating. Technol. 260 (2014) 214–219, https://doi.org/10.1016/j.surfcoat.2014.07.091.

[32] Y.C.K. Chen-Wiegart, F.E. Camino, J. Wang, Sample preparation of energy materials for X-ray nanotomography with micromanipulation, ChemPhysChem 15 (2014) 1587–1591, https://doi.org/10.1002/cphc.201400023.

[33] M. Ge, D.S. Coburn, E. Nazaretski, W. Xu, K. Gofron, H. Xu, Z. Yin, W.K. Lee, One-minute nano-tomography using hard X-ray full-field transmission microscope, Appl. Phys. Lett. 113 (2018), https://doi.org/10.1063/1.5048378.

[34] D. Allan, T. Caswell, S. Campbell, M. Rakitin, Bluesky's ahead: a multi-facility collaboration for an a la Carte software project for data acquisition and management, Synchrotron Radiat. News 32 (2019) 19–22, https://doi.org/10.1080/08940886.2019.1608121.

[35] S.K. Abeykoon, Y. Zhang, E.D. Dill, T.A. Caswell, D.B. Allan, A. Akilic, L. Wiegart, S. Wilkins, A. Heroux, K.K. Van Dam, M. Sutton, A. Fluerasu, Software Tools for X-Ray Photon Correlation and X-Ray Speckle Visibility Spectroscopy, 2016 New York Sci. Data Summit, NYSDS 2016 - Proc, 2016, pp. 1–10, https://doi.org/10.1109/NYSDS.2016.7747815.

[36] M. Sutton, K. Laaziri, F. Livet, F. Bley, Using coherence to measure two-time correlation functions, Optic Express 11 (2003) 2268, https://doi.org/10.1364/oe.11.002268.

[37] A. Fluerasu, A. Moussaïd, A. Madsen, A. Schofield, Slow dynamics and aging in colloidal gels studied by x-ray photon correlation spectroscopy, Phys. Rev. E - Stat. Nonlinear Soft Matter Phys. 76 (2007) 3–6, https://doi.org/10.1103/PhysRevE.76.010401.

[38] A. Madsen, R.L. Leheny, H. Guo, M. Sprung, O. Czakkel, Beyond simple exponential correlation functions and equilibrium dynamics in x-ray photon correlation spectroscopy, New J. Phys. 12 (2010), https://doi.org/10.1088/1367-2630/12/5/055001, 0–16.

[39] G. Williams, D.C. Watts, Non-symmetrical dielectric relaxation behaviour arising from a simple empirical decay function, Trans. Faraday Soc. 66 (1970) 80–85, https://doi.org/10.1039/TF9706600080.

[40] A. Duri, L. Cipelletti, Length scale dependence of dynamical heterogeneity in a colloidal fractal gel, Europhys. Lett. 76 (2006) 972–978, https://doi.org/10.1209/epl/i2006-10357-4.

[41] V. Trappe, E. Pitard, L. Ramos, A. Robert, H. Bissig, L. Cipelletti, Investigation of q -dependent dynamical heterogeneity in a colloidal gel by x-ray photon correlation spectroscopy, Phys. Rev. E - Stat. Nonlinear Soft Matter Phys. 76 (2007) 1–7, https://doi.org/10.1103/PhysRevE.76.051404.

[42] E.M. Herzig, A. Robert, D.D. Van'T Zand, L. Cipelletti, P.N. Pusey, P.S. Clegg, Dynamics of a colloid-stabilized cream, Phys. Rev. E - Stat. Nonlinear Soft Matter Phys. 79 (2009) 1–7, https://doi.org/10.1103/PhysRevE.79.011405.

[43] L. Cipelletti, H. Bissig, V. Trappe, P. Ballesta, L. Cipelletti, H. Bissig, V. Trappe, P. Ballesta, S.M.T. Re, Time Resolved Correlation : a New Tool for Studying Temporally Heterogeneous Dynamics to Cite This Version : Time Resolved Correlation : a New Tool for Studying Temporally Heterogeneous Dynamics, 2005.

[44] B. Abou, D. Bonn, J. Meunier, Aging dynamics in a colloidal glass, Phys. Rev. E 64 (2001) 6, https://doi.org/10.1103/PhysRevE.64.021510. Stat. Physics, Plasmas, Fluids, Relat. Interdiscip. Top.

[45] L. Cipelletti, L. Ramos, Slow dynamics in glasses, gels and foams, Curr. Opin. Colloid Interface Sci. 7 (2002) 228–234, https://doi.org/10.1016/S1359-0294(02)00051-1.

[46] D. Orsi, L. Cristofolini, G. Baldi, A. Madsen, Heterogeneous and anisotropic dynamics of a 2D Gel, Phys. Rev. Lett. 108 (2012) 1–5, https://doi.org/10.1103/PhysRevLett.108.105701.

[47] A.H. Krall, D.A. Weitz, Internal dynamics and elasticity of fractal colloidal gels, Phys. Rev. Lett. 80 (1998) 778–781, https://doi.org/10.1103/PhysRevLett.80.778.

[48] A. Grein-lankovski, I.C. Riegel-Vidotti, F.F. Simas-Tosin, S. Narayanan, R.L. Leheny, A.R. Sandy, Exploring the relationship between nanoscale dynamics and macroscopic rheology in natural polymer gums, Soft Matter 12 (2016) 9321–9329, https://doi.org/10.1039/c6sm01492e.

[49] G. Grübel, A. Madsen, A. Robert, X-ray photon correlation spectroscopy (XPCS), in: R. Borsali, R. Pecora (Eds.), Soft Matter Charact., Springer Netherlands, Dordrecht, 2008, pp. 953–995. http://scripts.iucr.org/cgi-bin/paper?S1600577514018232.

[50] P. Kwaśniewski, A. Fluerasu, A. Madsen, Anomalous dynamics at the hard-sphere glass transition, Soft Matter 10 (2014) 8698–8704, https://doi.org/10.1039/c4sm01671h.

[51] L. Cipelletti, S. Manley, R.C. Ball, D.A. Weitz, Universal aging features in the restructuring of fractal colloidal gels, Phys. Rev. Lett. 84 (2000) 2275–2278, https://doi.org/10.1103/PhysRevLett.84.2275.

[52] C. McIlroy, P.D. Olmsted, Deformation of an amorphous polymer during the fused-filament-fabrication method for additive manufacturing, J. Rheol. (N. Y. N. Y). 61 (2017) 379–397, https://doi.org/10.1122/1.4976839.

[53] A. M'Barki, L. Bocquet, A. Stevenson, Linking rheology and printability for dense and strong ceramics by direct ink writing, Sci. Rep. 7 (2017) 1–10, https://doi.org/10.1038/s41598-017-06115-0.

[54] L. Ramos, L. Cipelletti, Ultraslow dynamics and stress relaxation in the aging of a soft glassy system, Phys. Rev. Lett. 87 (2001), https://doi.org/10.1103/PhysRevLett.87.245503, 245503-1-245503–4.

[55] L. Cipelletti, L. Ramos, S. Manley, E. Pitard, D.A. Weitz, E.E. Pashkovski, M. Johansson, Universal non-diffusive slow dynamics in aging soft matter, Faraday Discuss 123 (2003) 237–251, https://doi.org/10.1039/b204495a.

[56] M. Bellour, A. Knaebel, J.L. Harden, F. Lequeux, J.P. Munch, Aging processes and scale dependence in soft glassy colloidal suspensions, Phys. Rev. E 67 (2003) 8,

https://doi.org/10.1103/PhysRevE.67.031405. Stat. Physics, Plasmas, Fluids, Relat. Interdiscip. Top.

[57] R. Bandyopadhyay, D. Liang, H. Yardimci, D.A. Sessoms, M.A. Borthwick, S.G.J. Mochrie, J.L. Harden, R.L. Leheny, Evolution of particle-scale dynamics in an aging clay suspension, Phys. Rev. Lett. 93 (2004) 2–5, https://doi.org/10.1103/PhysRevLett.93.228302.

[58] B. Chung, S. Ramakrishnan, R. Bandyopadhyay, D. Liang, C.F. Zukoski, J.L. Harden, R.L. Leheny, Microscopic dynamics of recovery in sheared depletion gels, Phys. Rev. Lett. 96 (2006) 3–6, https://doi.org/10.1103/PhysRevLett.96.228301.

[59] A. Robert, E. Wandersman, E. Dubois, V. Dupuis, R. Perzynski, Glassy dynamics and aging in a dense ferrofluid, Europhys. Lett. 75 (2006) 764–770, https://doi.org/10.1209/epl/i2006-10179-4.

[60] A. Madsen, A. Fluerasu, B. Ruta, Structural dynamics of materials probed by X-ray photon correlation spectroscopy, in: Synchrotron Light Sources Free.

Lasers, Springer International Publishing, Cham, 2016, pp. 1617–1641, https://doi.org/10.1007/978-3-319-14394-1_29.

[61] Aremco, Technical Bulletin A9 Aremco's Crystalbond ™. https://www.aremco.com/wp-content/uploads/2018/05/A09_18.pdf, 2018.

[62] A.L. Stancik, E.B. Brauns, A simple asymmetric lineshape for fitting infrared absorption spectra, Vib. Spectrosc. 47 (2008) 66–69, https://doi.org/10.1016/j.vibspec.2008.02.009.

[63] J.S. Pedersen, Analysis of small-angle scattering data from colloids and polymer solutions: modeling and least-squares fitting, Adv. Colloid Interface Sci. 70 (1997) 171–210, https://doi.org/10.1016/S0001-8686(97)00312-6.

[64] C. McIlroy, P.D. Olmsted, Disentanglement effects on welding behaviour of polymer melts during the fused-filament-fabrication method for additive manufacturing, Polymer 123 (2017) 376–391, https://doi.org/10.1016/j.polymer.2017.06.051.